Noname manuscript No.
(will be inserted by the editor)

To-and-fro motion of a submerged plate above an erodible bed

Román Martino · Ignacio Toriggia · Agnes Paterson · Marcelo Piva

Received: date / Accepted: date

Abstract The interaction between the oscillatory flow, driven by the to-and-fro translational movement of a vertical surface-piercing plate, and the (planar) granular bed is experimentally addressed. Focus is paid to the problem of the onset of sediment motion due to this interaction. By systematically varying the amplitude, A, and the frequency, f, as well as the gap between the lower tip of the plate and the bed, G, it is found that initiation of grains motion is mainly driven by the jet-like streams, spatially symmetrical, alternatively expelled after half-period through the gap, G. It was observed that grains are set into motion close to the center of the oscillatory motion, where the plate reachs its maximum velocity, $V_p = \pi A f$. Experimental points fall around a straight line when plotted in terms of the dimensionless numbers $\nu T_c/H^2$ and $\pi A_c/G_c$ (ν and H are kinematic viscosity and plate submergence, respectively, and $T_c = 1/f_c$), suggesting that the threshold condition is well defined by a roughly constant value of V_p/G. This findings are explained by means of a simple hydro-mechanical model, in terms of the (maximum) shear stress needed to dislodge a single grain overcoming the resistive force created by the submerged weight. Although limited to hydraulically smooth flow, the results presented here indicate that the phenomenon depends on geometric and strength parameters.

Keywords sediment transport · local erosion · critical shear stress · oscillatory flow

Román Martino · Ignacio Toriggia · Marcelo Piva
Grupo de Medios Porosos, Facultad de Ingeniería, Universidad de Buenos Aires, Paseo Colón 850 (1063), Buenos Aires, Argentina
Tel.: +5411-528-50841
E-mail: rmartino@fi.uba.ar

Román Martino
CONICET, Argentina

Agnes Paterson
Departamento de Hidráulica, Facultad de Ingeniería, Universidad de Buenos Aires, Las Heras 2214(1127), Buenos Aires Argentina

1 Introduction

Partially submerged plates, blades and foils, performing a to-and-fro motion normal to its surface, are commonly encountered in many structures and devices. For example, artificial floating constructions, such as wetlands or pontoons, often use a submerged vertical plate attached to the fore-end to damp hydrodynamic forces via wave energy dissipation [1]. The efficiency of such devices is improved by increasing the depth of the submerged plate. Another example is power generation using the motion of a flapping foil, that mimicks the motion of fish tails. It is a promising, emergent technology for very small scale installations, for example in remote communities (pyco-hydro power) [2]. In several designs the foil vertically penetrates the water stream, while it oscillates horizontally [3].

Most previous studies focused on the coupling between flow and the surface-piercing plate [4, 5, 6]: the determination of the hydrodynamics forces and the flow field structure are the main results from performance point of view. The case of a vertical plate piercing the air-water interface and moving forward, towed with a prescribed horizontal velocity, has received attention in studies of the juncture flow at the free surface line, where contact between water, air and the plate takes place [7, 8, 9]. The tip vortex structure has also received some attention, in connection with the interaction between vorticity, produced and shed at the lower edge of the plate, and the free surface. Under deep water conditions, in twodimensional configurations, three regimes were identified: subcritical, transitional and supercritical. In terms of the Froude number $Fr = V_p/\sqrt{gH}$, where V_p and H are the maximum velocity and the submergence of the plate, respectively, and g is gravitational acceleration, in subcritical regime ($Fr < 0.7$) no significant interaction takes place, whereas it can not be neglected in the supercritical regime ($Fr > 1$).

The interaction of waves and a surface-piercing body in water of finite depth has also been studied. When compared with the deep water case, a reduction in the water depth enhances all the wave-exciting forces [6]. Less attention has received the interaction between the flow, induced beneath the tip of the plate, and the bottom of the water body. This interaction, beyond its impact on operative efficiency, could be of major concern in presence of sedimentary beds, especially when the crafts operates in relatively shallow water environments. For example, stability of granular substrates could be compromised in the vicinity of the plate tip, with the risk of development of local erosion. Also, under certain operative conditions, water quality could be strongly affected by the resuspension of fine sediment. As a third example, remotion of grains from the bed can be accompanied by the release of bed-trapped contaminants, as heavy metals, compromising aquatic habitat [10].

The onset of sediment motion plays a central role in sediment transport theory and continues receiving attention from a basic point of view [11, 12, 13]. The phenomenon is present in many natural systems, as well as in several engineering and industrial applications [14, 15, 16]. In a unidirectional steady-uniform flow over a loose granular bed, the Shields criterion establishes that sediment transport will take place when the Shields number:

$$\theta = \frac{\tau}{(\rho_s - \rho) g d_s} \tag{1}$$

exceeds a critical threshold value, θ_c. In Eq. 1 τ is bed shear stress, ρ_s and ρ are sediment and fluid densities, respectively, g is gravitational acceleration and d_s is sediment diameter. A large body of work has been devoted to determine θ_c [17]. There are many other configurations where the onset of sediment motion needs to be determined. For example, water jets tangential to the granular bed can be used for sediment management [18]. The threshold of motion by water jets issuing from an orifice, or below a sluice gate, has been particularly studied [19, 20, 21].

The threshold of sediment motion in oscillatory flows, for example underwater waves in the ocean, is also an active field of research. In this case, currents are continuously varying and flow acceleration play an important role in particle detachment from the bed [22]. Based on experimental results obtained in oscillating trolleys and oscillatory-flow water tunnels, many empirical equations have been proposed to predict the entrainment threshold [23, 24, 25]. The analysis of the forces acting on the sediment particles highlights the key role played by the maximum horizontal velocity of the flow at the bed level, the wave period, p, and the size of the grains [26, 27]. It has been shown that rough bed processes dominate with particles larger than approximately $d_s > 2\ mm$, when eddies are shed from the grains [26, 28]. Vortex shedding from large oscillatory roughness elements feed the boundary layer, making this case markedly different when compared with non-oscillating flows [28, 29, 30].

In this contribution, the interaction between the reciprocating flow field driven by the back-and-forth motion of a vertically submerged plate, and the granular bed, is experimentally studied. Owing to the localized character of the flow beneath the plate, specific features regarding the onset of grains motion are expected. Focus is paid to the role played by the amplitude, A, and the frequency, f, the operative parameters defining the to-and-fro motion of the plate. In this sense, the experimental setup allows to impose well characterized oscillatory flows upon the planar granular layer. The influence of the distance between the bed and the lower tip of the plate, G, is also studied. Results are analyzed in terms of dimensionless numbers, used in the study of oscillating bodies submerged in a fluid. The main trends of the measurements can be explained by means of a simple model. The analysis show that incipient motion of sediment depends on strength parameters and geometrical variables. It is expected that the results will provide a sound basis for studying local erosion under partially submerged bodies undergoing oscillatory motions.

2 Experimental arrangement

2.1 Set-up

The experiments were performed in a rectangular narrow cell 60 cm long, 36 cm high and $w = 2\ cm$ in width, see Fig. 1. The cell was built by gluing two glass plates to a Plexiglas frame, and enclosed in a metallic support, to guarantee perfect horizontal and vertical alignment. The cell was filled with fresh water of density $\rho = 1\ g/cm^3$ and kinematic viscosity $\nu = 0.01\ cm^2/s$. The sedimentary bed is made of sieved sand with mean grain size $d_s = 0.2 \pm 0.02\ mm$ and density $\rho_s = 2.65\ g/cm^3$. By varying the height of the horizontal sandy layer, several values of the initial gap were considered, $5\ mm \leq G \leq 50\ mm$, with $\pm 1\ mm$ uncertainty. The cell

was illuminated from behind with a ligth panel, to ensure optimal contrast of the water-bed interface. The whole experimental setup was mounted in a room with black walls.

A thin stainless steel plate, 17 cm long, 3 mm thick and 19 mm wide, is vertically submerged $H = 13$ cm below the free surface, and performs a translational to-and-fro movement, normal to the surface of the plate. As seen in Fig. 1, a removable rooftop was placed on the top of the cell, with a small aperture in the central zone, where the plate performs the back-and-forth motion. A crank-connecting rod system was used to transform the rotary motion of a DC motor into a linear oscillatory movement. The upper end of the plate was rigidly joined to the horizontal rod (not shown in Fig. 1). By varying the crank length, several amplitudes were set in the range $4\ mm \leq A \leq 90\ mm$, with ± 1 mm uncertainty. The ratio between the crank length to the rod length was kept small to ensure the reciprocating motion of the plate is close to a sinusoidal motion. The driving system allowed to impose frequencies in the range $0.1\ Hz \leq f \leq 5\ Hz$, with $\pm 0,5\%$ uncertainty. Frequency was measured with an inductive proximity sensor, connected to a frequency meter.

2.2 The flow structure without sediment

The flow structure induced by the plate oscillation was first studied without the sediment, to remove the influence of the moving grains. The granular bed was replaced by a dummy adjustable bottom wall, covered with sandpaper of roughness close to that of the sand. The water was seeded with resin particles (Pliolite), density $1,03\ g/cm^3$ and $75 \pm 15 \mu m$ in size. The central streamwise section of the cell ($z = 0$) was illuminated with a laser sheet Neo-Yag 532 nm@ 100 mW, and recorded with a CCD monochrome camera. Initially, the fluid is motionless and, after the plate begins to oscillate, it takes several periods until the flow reaches its permanent state of motion.

For some combinations of the control variables, A and f, and moderate values of G, the flow was observed to be periodic in time and synchronous with the plate motion, see Fig. 2. This behavior is similar to those observed in previous studies of flow induced by oscillating bodies [31]. The seeded particles appears as traces rather than as bright spots in the pictures when the exposure time is set about 50 ms via the camera control software. The length and orientation of the traces are proportional to the fluid velocity at each point, so the snapshots reveal the structure of the instantaneous velocity field. The dark triangles near the lower corners are due to scarce illumination in this region.

Let consider a coordinate system whose origin is at the intersection between the center of the oscillation and the dummy bed level, and x and y are the horizontal and vertical axis, respectively. In Fig. 2(A), the plate is going toward the left, through $x = 0$, with the maximum speed. It is seen that the downward vertical flow along the left side of the plate bifurcates when it impinges the bed. One part of this vertical stream connects to the horizontal flow which passes below the plate and goes toward the right, whereas the other part feeds the large clockwise recirculation at the left side of the cell. On the right side, a counterclockwise vortex grows adjacent to the tip of the plate. More to the right, there is a counterclockwise circulation corresponding to a residual flow structure established in the previous semi-period. A significant reduction in the length of the traces is observed in the

area of contact between the tip vortex and the large recirculation. There, the shear stress between the two opposing flows generates a large energy dissipation, as a result of which there is an important reduction of the flow velocity in that region. Figure 2(B) shows the plate at the left end ($x = -A/2$), where the plate velocity is zero and the motion in the opposite direction is about to start. During the trajectory between $x = 0$ and $x = -A/2$, the tip vortex grew and traveled to the right, and is absorbed by the large recirculation. On the left side, the vertical flow and the bifurcation point are shifted toward the left, compressing the large clockwise circulation still present on that side. At the same time, a vertical downward flow is developing on the right side. The incipient formation of a bifurcation point dividing the vertical stream is also observed. The left stream beneath the plate, contributes to generate a vortex tip (barely noticeable in the picture) and also feeds the clockwise circulation that remains from the previous half cycle. On the right side, the large circulation, that was present in the previous figure, has now been completely replaced by the tip vortex. Figures 2(C) and (D) show the plate moving in the opposite direction, through $x = 0$ and arriving to the right end point, $x = A/2$, respectively. The same flow pattern than in Fig. 2(A) and (B) is observed, but symmetrical with respect to the vertical midplane of the oscillation.

Observations for a large number of experimental conditions show that, in broad terms, the flow morphology takes one of two possible configurations: spatio-temporally symmetric (STS) or temporally symmetric but spatially asymmetric (TSSA). The STS configuration is well described by the case of Fig. 2, where the symmetry properties of the velocity field, averaged across the transversal z-direction, can be written as:

$$(u, v)(x, y, t) = (-u, v)(-x, y, t + T/2) \tag{2}$$

being T the time period corresponding to the frequency of the oscillation f ($T = 1/f$). In the TSSA configuration, the flow on the two sides of the plate differs. On one side, the flow remains nearly motionless all the time (or with a slight reciprocating movement), except very close to the plate, where a tip vortex is generated. This vortex is expelled as a jet, every half period, to the opposite side, where a large recirculation is fed. The cross averaged velocity field can be written as:

$$(u, v)(x, y, t) = (u, v)(x, y, t + T/2) \tag{3}$$

A qualitative comparison between the two typical patterns is presented in Fig. 3. In both cases, snapshots in the bottom corresponds to the plate at the left end of its path, whereas top snapshots corresponds to the plate at the right end (x-inverted for comparison), after a half-period. Figure 3(A) shows the STS case: the flow structures are completely equivalent in size, shape and location, relative to the plate, confirming that symmetry properties of the flow field can be described by equation 2. Figure 3(B) shows that, unlike the previous case, the flow structure at both sides of the plate do not match after a half-period. The breakdown of the spatial symmetry indicates a transition to a TSSA case.

To further study the symmetry properties of the system, the position of the tip of the plate, x_p, and the center of the tip vortex, (x_v, y_v), were tracked as a

function of time, t. Figure 4 presents an example of the temporal evolution of x_p and x_v. The horizontal movement of the plate can be described by the relation:

$$x_p = A/2\cos(2\pi ft) \tag{4}$$

whereas two vortices are alternatively ejected from the tip of the plate every $\Delta t = T/2$. The vortex at the right side appears just after the plate inverts its motion, at point labeled (a). It is observed that the vortex has a rightward shift away from the plate and continues moving in the same direction when the plate begins its returning motion, at point labeled (b). A few moments later, when the tip vortex absorbs the large recirculation (as seen in Figures 2(C) and (D)) it slows down because it has grown filling the available space of the container, at point labeled (c). In the meanwhile, at point (b), the plate has initiated its rightward motion and the tip vortex of the left side begins to grow toward the point (d). The vortices performs similar paths at both sides but in opposite directions. In this case, the system has the spatio-temporal symmetry, STS, described by Eq. 2.

Figure 5 shows the trajectory of the center of the tip vortex. The coordinates (x_v, y_v) were tracked during several oscillations to show the periodic nature of the flow field. The upper plot corresponds to the flow conditions shown in Fig. 4. The slight dispersion of data around the main trend (pointed out by gray continuous lines drawn above the experimental points) reflects the limitation of the tracking program to find the coordinates. However, it is clear that the right side vortex originates at the point labeled (a), it moves to the right, in a quasi-horizontal path, and deviates upward, toward the end of its motion, at the point labeled (c). The path of the left side vortex is equivalent in shape and size, but in the opposite direction. The lower plot of Fig. 5 shows the tip vortex paths in a TSSA configuration. The right side vortex originates just as the plate passes through $x = 0$ moving towards the left, and then follows a slightly wavy, but almost horizontal, path toward the right. The left side vortex moves toward the left but with a clearly different path. The flow field still exhibits temporal periodicity, but the spatial symmetry about the center of the oscillation is gone. Thus, its symmetry properties are well described by Eq. 3.

Based on the above described procedures, the overall structure of the flow (TSS or TSSA) was identified for a large number of configurations, by systematically varying the values of A, f and G. Four values of G were used: 10, 20, 30 and 40 mm. For each value of G, twelve values of A were studied in the range $4 \leq A \leq 54$ mm. For given values of G and A, forty values for f, between 0.1 and 4 Hz, were explored, thus covering a broad range of flow configurations. Results were analyzed by means of dimensional analysis (Π theorem), to organize and classify the measurements in regions of STS or TSSA behavior. By assuming that $V_p = 1/2A\omega = \pi Af = \pi A/T$ is the suitable velocity scale and that a functional relationship between V_p, G, H and ν exists, then two dimensionless numbers are needed to describe the phenomenon.

In most of the studies about submerged oscillating cylinders of radius R, very often is used the so-called Stokes viscous parameter, $\nu T/R^2$. This number, obtained from the ratio between the viscous forces and the oscillatory inertial forces, play a key role for characterizing flow patterns around submerged oscillating bodies, together with the Keulegan-Carpenter number, defined from the ratio between the amplitude and R [32, 33]. This last number quantifies the relative importance

of convective accelerations with respect to the local accelerations of the flow. By assuming that viscous forces effects are dominant along the length of the plate, H, the ratio of viscous to inertial forces, P, is defined as:

$$P = \frac{\mu \nabla^2 U}{\rho \partial U/\partial t} \sim \frac{\nu U/L^2}{U/T} = \frac{\mu V_p/H^2}{\rho V_p/T} = \frac{\nu T}{H^2} \tag{5}$$

which is the ratio between the viscous diffusion time over the distance H and the period T. Regarding the second number, if it is assumed that velocity gradients scale with V_p/G, then the ratio of convective to local accelerations, S, is given by:

$$S = \frac{U.\nabla U}{\partial U/\partial t} \sim \frac{U^2/L}{U/T} \sim \frac{U/L}{1/T} = \frac{V_p/G}{1/T} = \pi \frac{A}{G} \tag{6}$$

Since measurements were based on the identification of flow structures (STS or TSSA), this numbers will be useful to lay out a phase diagram. Figure 6 presents the data in a graph with P in abcissa and S in ordinates. In general terms, for $S > 4,8$ ($A > 1.5G$), approximately, the flow is STS irrespective the values of P. In the range $0 \leq S \leq 4,8$, the flow can be STS or TSSA, this latter represented as a gray region in the figure. Thus, a plate undergoing a back-and-forth motion with relatively low values of S and P can develop and sustain a TSSA flow structure. The small STS region, bounded around the origin of coordinates by the TSSA gray zone, corresponds to a marginal behaviour of STS flow, where no vortex shedding was observed, and the bulk of fluid performs a to-and-fro motion as a whole, synchronous to the plate motion. The peak at $P \approx 0.000034$ (corresponding to $f \approx 1,6\ Hz$) is probably associated with a resonant coupling coming from the interaction between the periodic forcing by the oscillating plate and the natural frequency of the liquid in the cell. This phenomenon, entirely due to the finite dimensions of the container, is beyond the scope of this study. From Fig. 6 it is concluded that there exists a broad region in the $P - S$ plane where STS flows are present. As it will be shown in the next Section, most of the critical points for onset of sediment motion were registered under STS flows.

3 Threshold for sediment motion

To determine the critical combination of frequency, f, amplitude, A, and gap, G, needed to initiate the motion of the grains, the container was partly filled with sand, and the surface was smoothed to set the desired value of G. Then, a value of f, close to the threshold, was imposed for a preset value of A. In this condition, the plate was allowed to oscillate during 15 minutes. The camera took two pictures, one at $t = 0$ and one at $t = 15\ min$. The frequency was then increased by small intervals of about $\Delta f \approx 0.01\ Hz$, and the procedure was repeated. Each pair of images was compared by digital subtraction. For frequencies below the critical value, $f < f_c$, the shear stress on the bed surface is too small to initiate the grains motion, and the result of the subtraction is a dark picture. On the contrary, if $f > f_c$, the shear stress overcome bed resistance and there are grains set in motion, and the resulting picture displays a bright zone at the interface between the granular bed and the liquid. At the critical frequency, f_c, the bright zones decrease to a 1 pixel thickness. With this procedure the uncertainty of f_c is about $\pm 0.01\ Hz$.

Figure 7 displays the results obtained for two different frequencies. Each column displays three snapshots: the upper one corresponds to the (initially flat) sandy bed, the central one is an image taken 15 minutes after the plate started moving, and the bottom one is the digital difference between the two former ones. In the left column, for $f > f_c$, the local erosion of the bed is clearly visible: a scour hole and two lateral (symmetrical) mounds appear as light areas. Naked-eye observations showed that, at the earlier stages, grains were expelled as bursts every time the plate passed through the vicinity of $x \approx 0$, where V_p peaks. The amount of grains being transported was found to increase as V_p increase. Grains mainly moved as bedload, rolling in the opposite direction to the plate motion. As the hole deepens, the rate of sediment transport slowed down and the erosive process decelerates. In the right column, the snapshots at $t = 0$ and at $t = 15\ m$ look identical at first glance. However, naked-eye observation showed that few grains were "trembling". Eventually, some of them were dislodged and moved a short distance. These small desplacements appear in the sustracted image as very thin bright lines on the bed surface, revealing the system is very close to the onset of grains motion ($f \approx f_c$).

By applying the above procedure several sets of critical triplets (G_c, A_c, f_c) were determined, see Fig. 8. On the one hand, for a given G, it is observed that as A increases, the critical frequency needed to dislodge grains and put them into motion decrease. On the other hand, for a given A, the critical frequency increases with G. Figure 9 shows that the experimental points from Fig. 8 fall around a straight line, when they are plotted in terms of the dimensionless numbers S and P, evaluated at the critical condition (with $T_c = 1/f_c$). In the same plot are also included the bounds of the flow regimes STS and TSSA (see Fig. 6). Aside from a very few points, it is concluded that the threshold for sediment motion occurs under STS flows. In spite of some scatter of the data (which we will seek to reduce, by introducing corrections in the following part of this work) the proportionality between S_c and P_c is evident. This has a direct physical interpretation: using Eqs. 5 and 6 it is obtained $Af/G \simeq$ constant at the onset of grains motion. Inasmuch as Af is the velocity scale, and G the heigth above the bed where large velocity gradients occur, then Af/G is the scale for the gap-averaged shear rate. Hence, the onset of fines motion must be attributed, in first approximation, to the action of bed shear stress, $\mu Af/G$, where $\mu = \nu\rho$ is fluid viscosity. Accordingly, the jets alternatively expelled tangential to the bed each half a cycle appear to be the main contributors to the forces responsible of initiation of sediment motion. In the following Section, this hypothesis is used to develop a quite simplified model (Shields criterion), in terms of the maximum shear stress upon the bed. This rough approximation, linking the motion of the plate with the mean flow issuing below it, allows to explain the trend of the experimental data.

4 Discussion

The threshold of sediment motion can be evaluated in terms of the critical shear stress, τ_c, needed to dislodge a single grain from the bed. From the balance between the (destabilizing) hydrodynamic force over one grain and the stabilizing effect of its submerged weight, and neglecting the lift force [13], the critical Shields number is obtained [17]:

$$\theta_c = \frac{\tau_c}{\Delta \rho g d_s} \tag{7}$$

which is fundamental in studies regarding initiation of sediment motion. The Shields diagram presents θ_c as a function of the dimensionless diameter $d^* = d_s((\rho_s/\rho - 1)g/\nu^2)^{1/3}$ [34, 35]. In the present work, with $d^* \approx 5$ it is $\theta_c \approx 0.055$.

To estimate the hydrodynamic tractive force, the mean velocity field beneath the plate was measured with PIV using the same materials and equipments described in subsection 2.2. Measurements were performed under STS flow regime, since the onset of grains motion occurs mostly within this region of the $P - S$ plane. Due to limitations in image capture speed (< 200 fps), measurements were restricted to the low frequency regime ($< 1\ Hz$). Figure 10 presents a typical result for $G = 20\ mm$, $A = 10\ mm$ and $f = 0.5\ Hz$. In the left plot, the plate is passing through $x = 0$ while it is moving towards the left. Below the plate the fluid moves to the right with its maximum velocity. As it was already discussed in Fig 2(A), a stagnation point at $x \approx -10\ mm$ and the tip vortex at the right side are clearly visible. In spite of the distortion of the flow field, it is observed that the jet-like current runs almost horizontal immediately above the bed. The plot at the right in Fig. 10 shows the flow field when the plate arrives to the left end of its path (zero velocity point). The vortical structure has been shed to the right whereas the stagnation point has moved slightly to the left, as it was discussed in Fig. 2(B), and the flow field just above the bed remains mainly horizontal.

The above results suggests that the mean flow in the gap G can be roughly described as an horizontal jet, whose direction changes after a half-period. Figure 11(A) presents profiles of the longitudinal component of the flow field, $u(0, y)$, at $x = 0$ and for several couples of values of A and f. In all cases, similar trends are observed: the velocity quickly reaches a close to constant value at a small height above the bed, and the plateau of velocity extends over almost the entire gap, except close to the tip of the plate, where flow velocity decreases and takes negative values, so that $u(0, G) \approx V_p = \pi A f$ directed towards the left. The noticeable feature is the organizing role of V_p on the values of the velocity profiles. Indeed, U, the mean flow velocity (estimated by averaging the points in the plateau of the profiles), is proportional to V_p, as shown in Table 1. This can be supported by means of a simple model. Due to mass conservation, as the plate moves towards one side, all the volume of fluid is swept and passes beneath the plate towards the opposite side. In rough terms, a mean value of the horizontal flow velocity, U_F, can be defined as the mean fluid volume crossing the gap G per unit time and surface:

$$U_F = \frac{\Delta V}{\Delta t S} = \frac{H V_p}{G} = \frac{H \pi A f}{G} \tag{8}$$

where $\Delta V = H V_p \Delta t w$ is the volume swept by the plate during Δt and $S = wG$ is the area of the surface below the plate ($w = 2\ cm$ is the cell width and $H = 13\ cm$ the plate length). The estimation of U_F is given in Table 1. In spite of the rough approximation, U_F compares well with U, obtained from the experimental profiles. The role of U_F as a suitable velocity scale is reinforced by plotting u/U_F against y/G. Figure 11(B) shows that points groups along a single curve. Although some scatter exists at the top of the profiles (where the vortex shedding takes place),

run	$G\ (mm)$	$A\ (mm)$	$f\ (Hz)$	$V_p\ (cm/s)$	$U\ (cm/s)$	$U_F\ (cm/s)$
1	20	10	0.25	0.8	4.8	5.1
2	20	10	0.50	1.6	8.5	10.2
3	20	18.9	0.25	1.5	8.5	9.6
4	20	29.1	0.25	2.3	11.4	14.9

Table 1 Summary of experimental conditions for PIV measurements.

close to the bed the collapse is quite satisfactory. Interestingly, U_F can be written in terms of S and P, see Eqs. 5 and 6:

$$U_F = \frac{H\pi Af}{G} = \frac{\nu}{H}\frac{S}{P} \tag{9}$$

Thus, based on the criterion of maximum bed shear stress, used in quasi-stationary models for sediment transport under oscillatory flows [26, 36], and since the plate velocity peaks close to the center of the oscillation ($x = 0$), τ_c is calculated as follows:

$$\tau_c = \frac{f_D}{8}\rho U_{F_c}^2 \tag{10}$$

where f_D is the Darcy friction coefficient [37]. The critical Reynolds number, calculated as:

$$Re_c = \frac{U_{F_c} D}{\nu} \tag{11}$$

where $D = 4wG/(2w + 2G)$ is the hydraulic diameter between the tip of the plate and the bottom of the channel, ranged between $1480 \leq Re_c \leq 5400$. The flow is fully laminar for $Re_c \leq 2000$, approximately, and is transitional in the range $2000 < Re_c \leq 5000$. Previous works have shown that, under sinusoidal flows, smooth bed processes dominate for $d_s < 0.05\ cm$ [28], and that, for grains diameter less than about this size, the onset of motion occurs while the boundary layer is still laminar [26]. In this conditions, the friction coefficient is a function of Reynolds number only. In laminar flow it may be estimated by $f_D = 64/Re_c$. Thus, by replacing in Eq. 10, it follows:

$$\tau_c = \frac{64\nu}{8U_{F_c}D}\rho U_{F_c}^2 = \theta_c \Delta\rho g d_s \tag{12}$$

Replacing Eq. 9 in Eq. 12, and rearranging terms, it is obtained:

$$\frac{S_c}{P_c} = \frac{1}{4}\theta_c \frac{\Delta\rho}{\rho}\frac{g d_s H^2}{\nu^2}\frac{1}{\left(\frac{H}{w} + \frac{H}{G}\right)} = \phi_1 \tag{13}$$

which implies the following general expression:

$$S_c = \phi_1(\sigma, \eta) P_c \tag{14}$$

where σ, given by:

$$\sigma = \theta_c \left(\frac{\rho_s}{\rho} - 1\right)\frac{g d_s H^2}{\nu^2} \tag{15}$$

can be interpreted as a strength paramter, and η, defined as:

$$\eta = \frac{H}{w} + \frac{H}{G} \tag{16}$$

is an aspect ratio number, which combines the geometrical scales of the problem: the gap aspect ratio, H/G, and the plate aspect ratio, H/w.

In the transitional flow regime, the friction coefficient, f_D, may be estimated using the Wilson-Azad formula [38]: $f_D = 56.8 \cdot 10^{-10} Re_c^2$. By inserting this expression in the Eq. 10, it follows:

$$\tau_c = \frac{56.8 \cdot 10^{-10} U_{F_c}^2 D^2}{8\nu^2} \rho U_{F_c}^2 = \theta_c \Delta \rho g d_s \tag{17}$$

Replacing Eq. 9 in Eq. 17, and after some algebra, it follows:

$$\frac{S_c}{P_c} = \left[\frac{2}{56.8 \cdot 10^{-10}} \theta_c \frac{\Delta\rho}{\rho} \frac{g d_s H^2}{\nu^2} \left(\frac{H}{w} + \frac{H}{G} \right)^2 \right]^{1/4} = \phi_2 \tag{18}$$

Similarly to Eq. 13, the Eq. 18 can be written as:

$$S_c = \phi_2(\sigma, \eta) P_c \tag{19}$$

where $\phi_2(\sigma, \eta)$ is a dimensionless function of σ and η, given by Eqs. 15 and 16.

In summary, the threshold of sediment motion can be written as:

$$S_c = \phi(\sigma, \eta) P_c \tag{20}$$

with $\phi(\sigma, \eta)$ a dimensionless function, given by:

$$\phi(\sigma, \eta) = \begin{cases} \phi_1(\sigma, \eta), & Re_c < 2000 \text{ laminar flow} \\ \phi_2(\sigma, \eta), & 2000 < Re_c < 5000 \text{ transitional flow} \end{cases} \tag{21}$$

The Figure 12 shows that the experimental results plotted in terms of S_c and $\phi(\sigma, \eta) P_c$ fall along a straight line with intercept 0 and slope 1, in accordance with Eq. 20. Although some scatter is still present, the correction clearly improves the correlation showed in Fig. 9, with data points falling closer to the unity line. The absence of adjustable parameters confirms the relevance of the underlying assumptions. Although rather crude, the approach higlights the role of the many variables influencing the problem. In particular, it shows that the strength number, σ, and the aspect ratio number, η, see Eqs. 15 and 16, are helpful parameters to organize experimental data.

Based on the definition of σ, the sediment size d_s, is expected to play an important role in sediment transport induced by reciprocating flows. Indeed, at the bed level, large particles need high flow velocities to be dislodged, leading the flow to become turbulent. The development of turbulence in oscillating flows is regulated by the balance between fluid acceleration, sources of flow perturbation, velocity distribution and timescales [28]. Laminar-to-turbulent transition over relatively smooth beds is initiated when destabilizing shear in the vertical profile of horizontal velocity becomes larger than stabilizing forces. Over very rough beds, initial flow perturbation is caused primarily by eddies shed from individual roughness elements [26, 28, 29]. Thus, in hydraulically rough beds the viscous-damping effect

is absent. Besides, under the accelerating phase of the oscillating boundary layer flow above large roughness elements, lift forces need to be included in the analysis [22, 30].

Further research is needed to overcome limitations of the present model. For instance, under low submergence regimes ($Fr = V_p/\sqrt{gH} > 1$), the interaction between the lower tip vortex and the free surface, affects the flow field structure [9] and, so, the onset of sediment motion. Indeed, tridimensional effects arising from the corner vortices developed downstream of the moving plate could also be of importance [5]. Previous work on curvature-induced streamwise vortices shown that the turbulence created by these structures contribute to increase the total shear stress on the bed [39].

5 Conclusions and perspectives

The experiments reported here examined the interaction between the reciprocating flow, driven by the (horizontal) back-and-forth motion of a surface-piercing vertical plate, and a horizontal (planar) layer of fine sand. Attention was focussed on how the threshold for initiation of sediment motion is affected by the amplitude, A, and the frequency, f, of the plate motion, as well as the gap between the tip of the plate and the bed, G.

Velocimetry by tracking neutrally-buoyant tracer particles revealed that jet-like streams, tangential to the bed, are alternatively expelled in the gap G, every half-period of the plate motion, accompanied by an intense tip vortex shedding. Results shown that the maximum mean velocity of the flow beneath the plate, $U_F = (H/G)V_p$, is reached at the center of the reciprocating motion, $x \approx 0$, corresponding to the peak of the translational velocity of the plate, $V_p = \pi A f$. Most of the studied configurations had this spatio-temporally-symmetric (STS) structure.

For conditions slightly above the threshold of motion it was observed that, each time the plate passed through $x \approx 0$, grains were expelled as a burst in the opposite direction. The amount of removed sediment increased with U_F. Most of the grains move as bedload and, after travelling a short distance, they accumulate in a mound-like structure. This results indicates that grains motion is mainly driven by shear forces tangential to the bed.

The onset of sediment motion, measured by an image-substraction techique, occurs at an almost constant value of the ratio Af/G. This result was explained in terms of the maximum shear stress, τ_c, due to the horizontal tractive force needed to dislodge a single grain overcoming the bed resistence. Since τ_c was not measured in these experiments, it was defined in terms of U_F and the friction coefficient. Incipient motion was postulated to occur when $\tau_c/((\rho_s - \rho)gd_s) \approx \theta_c$, where θ_c is the critical Shields number obtained from the Shields diagram. The results indicate that the phenomenon depends on geometric and strength parameters. Dimensionless numbers σ and η, see Eqs. 15 and 16, could be of interest in further studies regarding the complex interaction between partially sumberged bodies and a granular substrate, especially when they operate in relatively shallow water environments.

Further research is needed to study how this findings change with the sediment size, d_s. Results reported here correspond to hydraulically smooth flow regime, where viscous effects in the boundary layer tend to be dominant, and friction is

mainly dependent on the Reynolds number, $Re = U_F D/\nu$. In hydraulically rough beds friction depends weakly on Re and mainly on the relative roughness, d_s/D. Moreover, larger particles under turbulent flows may lead to initiation of motion whithin non symmetric flow regimes. This is based on preliminary measurements under net transport regime, where symmetrical and non-symmetrical erosive structures were observed, the selection being guided by the regime and the structure of the reciprocating flow.

Acknowledgment

The authors gratefully acknowledge the financial support from Universidad de Buenos Aires (UBACyT 20020100100853). The authors would also like to thank M. A. Aguirre and J-P. Hulin for their helpful comments and suggestions.

References

1. C. M. Wang, Z. Y. Tay, K. Takagi and T. Utsunomiya, "Literature Review of Methods for Mitigating Hydroelastic Response of VLFS Under Wave Action", Applied Mechanics Reviews (ASME) 63/030802 1-18 (2010).
2. A. C. Fernandes and A. B. Rostami, "Hydrokinetic energy harvesting by an innovative vertical axis current turbine", Renewable Energy 81, pp. 694-706 (2015).
3. J. Young, J.C.S. Lai and M.F. Platzer, "Flapping Foil Power Generation: Review and Potential in Pico-Hydro Application", International Conference on Sustainable Energy Engineering and Application, IEEE, pp. 95-100 (2015).
4. K. Klaka, J.D. Penrose, R.R Horsley and M.R. Renilson, "Hydrodynamic tests on a fixed plate in uniform flow", Experimental Thermal and Fluid Science 30, pp. 131139 (2005).
5. P. Martinez-Legazpi, J. Rodriguez-Rodriguez, C. Marugan-Cruz and J. C. Lasheras, "Plunging to spilling transition in corner surface waves in the wake of a partially submerged vertical plate", Exp Fluids 54:1437 (2013).
6. Lixian Wang, Hui Tanga and Yanhua Wub, "Wave interaction with a surface-piercing body in water of finite depth: a parametric study", Engineering Applications of Computational Fluid Mecanics 10(1), pp. 512528 (2016).
7. V. I. Bukreev and A. V. Gusev, "Waves ahead of a vertical plate in a channel", Fluid Dynamics 34(1), pp 7177 (1999)
8. W-T. Tsai and D. K. P. Yue, "Interactions between a free surface and a vortex sheet shed in the wake of a surface-piercing plate, J. Fluid Mech. 257, pp. 691-721 (1993).
9. G. Colicchio, M. Landrini and J. R. Chaplin, "Level-Set Computations of Free Surface Rotational Flows", Journal of Fluids Engineering (ASME) 127, pp. 1111-1121 (2005)
10. Kalnejais, L., Martin, W., Signell R. and Bothner, M., "Role of sediment resuspension in the remobilization of particulate-phase metals from coastal sediments", Environ. Sci. Technol., 41(7): 2282-2288 (2007).

11. M. Houssais, C. P. Ortiz, D. J. Durian and D. J. Jerolmack, "Onset of sediment transport is a continuous transition driven by fluid shear and granular creep", Nature Communications 7527, pp. 1-8 (2015).
12. A. H. Clark, M. D. Shattuck, N. T. Ouellette and C. S. OHern, "Onset and cessation of motion in hydrodynamically sheared granular beds", Physical Review E 92, 042202 (2015).
13. A. Hong, M. Tao and A. Kudrolli, "Onset of erosion of a granular bed in a channel driven by fluid flow", Physics of Fluids 27, 013301 (2015).
14. F. B. Soepyan, S. Cremaschi, B. S. McLaury, C. Sarica, H. J. Subramani, G. E. Kouba, H. Gaod, "Threshold velocity to initiate particle motion in horizontal and near-horizontal conduits", Powder Technology 292, pp. 272289 (2016).
15. S. Dey, "Entrainment Threshold of Loose Boundary Streams", Experimental Methods in Hydraulic Research, Geoplanet: Earth and Planetary Sciences, P. Rowinski (ed.), Springer-Verlag Berlin (2011).
16. D. Dasani, C. Cyrus, K. Scanlon, R. Du, K. Rupp, K. H. Henthorn, "Effect of particle and fluid properties on the pickup velocity of fine particles", Powder Technology 196, pp. 237240 (2009).
17. S. Z. Ali and S. Dey, "Hydrodynamics of sediment threshold", Physics of Fluids 28, 075103 (2016).
18. O. Sequeiros, M. Cantero and M. H. García, "Sediment management by jets and turbidity currents with application to a reservoir for flood and pollution control in Chicago, Illinois", Journal of Hydraulic Research 47 (3), pp. 340348 (2009).
19. A. J. Hogg, H. E. Huppert and W. B. Dade, "Erosion by planar turbulent wall jets", J. Fluid Mech. 338, pp. 317-340 (1997).
20. R. Balachandar and H. P. Reddy, "Scour Caused by Wall Jets", Sediment Transport Processes and Their Modelling Applications, Andrew Manning (Ed.), ISBN 980-953-307-557-5, pp. 177-210 (2012).
21. S. Badr, G. Gauthier and P. Gondret, "Erosion threshold of a liquid immersed granular bed by an impinging plane liquid jet", Physics of Fluids 26, 023302 (2014).
22. D. Frank, D. Foster, I. M. Sou, J. Calantoni and P. Chou, "Lagrangian measurements of incipient motion in oscillatory flows", J. Geophys. Res. Oceans 120, pp. 244256 (2015).
23. M. A. Losada and J. M. Desir, "Incipient motion on a horizontal granular bed in non-breaking water waves", Coastal Engineering 9(4), pp. 357-370 (1985)
24. Z-J. You, "Initial Motion of Sediment in Oscillatory Flow", Journal of Waterway Port Coastal and Ocean Engineering (ASCE) 124(2) (1998).
25. J.P. Le Roux, "Entrainment threshold of sand-to granule-sized sediments under waves", Sedimentary Geology 322, pp. 6366 (2015).
26. P. Komar and M. Miller, "Sediment Threshold under Oscillatory Waves", Coastal Engineering 1974: pp. 756-775 (1974).
27. K. She, L. Trim and D.J. Pope, "Threshold of Motion of Natural Sediment Particles in Oscillatory Flows", Journal of Coastal Research 22(3), pp. 701709 (2006).
28. D. O. Lambkin, M. B. Collins and D. Paphitis, "Wave period and flow asymmetry effects on the transition to turbulence in relation to sediment dynamics", J. Geophys. Res., 109, F03009 (2004).

29. R.V. Krstic and H.J.S. Fernando, "The nature of rough-wall oscillatory boundary layers", Journal of Hydraulic Research, 39(6), pp. 655-666 (2001).
30. F. Fornarelli and G. Vittori, "Oscillatory boundary layer close to a rough wall", European Journal of Mechanics B/Fluids 28, pp. 283.295 (2009).
31. J. Yang, X. Tian and X. Li, "Hydrodynamic characteristics of an oscillating circular disk under steady in-plane current conditions", Ocean Eng. 75, pp. 5363 (2014).
32. Tian, X., Tao, L.,Li, X. and Yang, J., "Hydrodynamic coefficients of oscillating flat plates at $0.15 \leq KC \leq 3.15$", J. Mar. Sci. Technol. 22:101 (2017).
33. A. W. Troesch and S. K. Kim, "Hydrodynamic forces acting on cylinders oscillating at small amplitudes", Journal of Fluids and Structures 5, pp. 113-126 (1991).
34. J. Guo, "Hunter Rouse and Shields diagram", Advances in Hydraulics and Water Engineering, Proc. 13th IAHR-APD Ccongress, Vol. 2, World Scientific, Singapore (2002).
35. A.A. Beheshti and B. Ataie-Ashtiani, "Analysis of threshold and incipient conditions for sediment movement", Coastal Engineering 55, pp. 423430 (2008).
36. M. Janssen, "Sand transport in oscillatory sheet-flow: a literature review", Communications on Hydraulics and Geotechnical Engineering, Report No. 95-6, Faculty of Civil Engineering, Delft University of Technology, ISSN 0169-6548 (1995).
37. F. White, Fluid Mechanics, 1st. Ed., McGraw-Hill (1979).
38. N. W. Wilson and R. S. Azad, "A continuous prediction method for fully developed laminar, transitional and turbulent flows in pipes", ASME. J. Appl. Mech., 42, pp. 51-54 (1975).
39. E. Hopfinger, W. Graf and U. Lemmin, "Sediment erosion by Grtler vortices: The scour-hole problem", Journal of Fluid Mechanics 520, pp. 327-342 (2004).

List of Figures

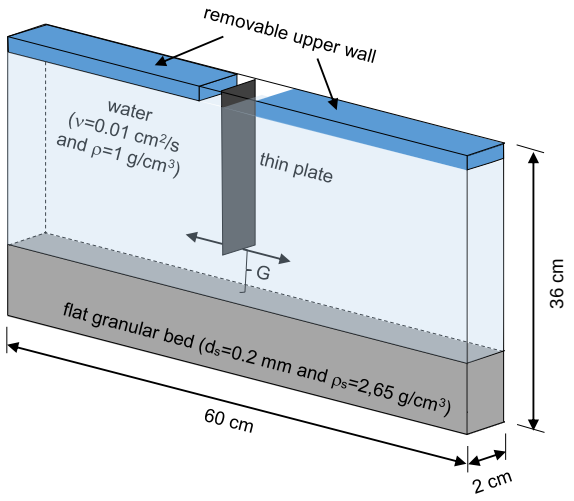

Fig. 1 Skecth of the experimental setup.

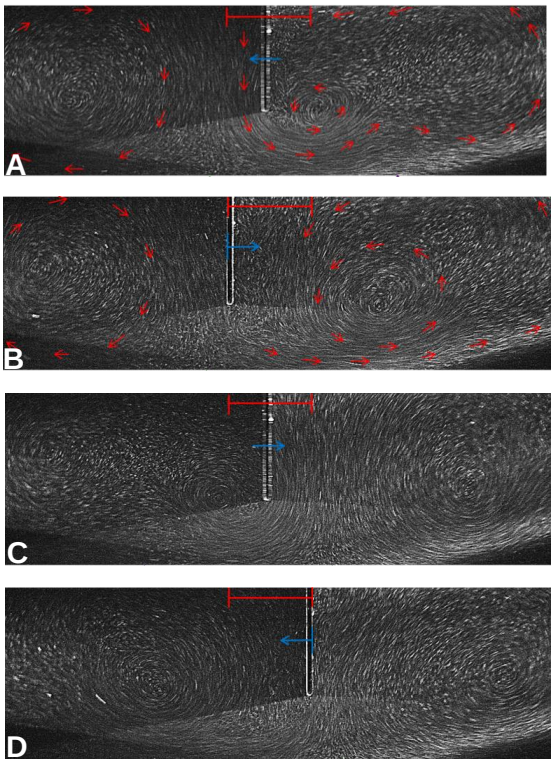

Fig. 2 Example of symmetrical flow patterns in a complete cycle of plate motion above an horizontal, rough and non-erodible bed: (A) the plate is at the center of the cell ($x = 0$) and is moving to the left (B) the plate is at the left end of its oscillatory motion, ($x = -A/2$) (C) and (D) flow patterns are a reflection, about the y-axis of the container, from those shown in the pictures (A) and (B).

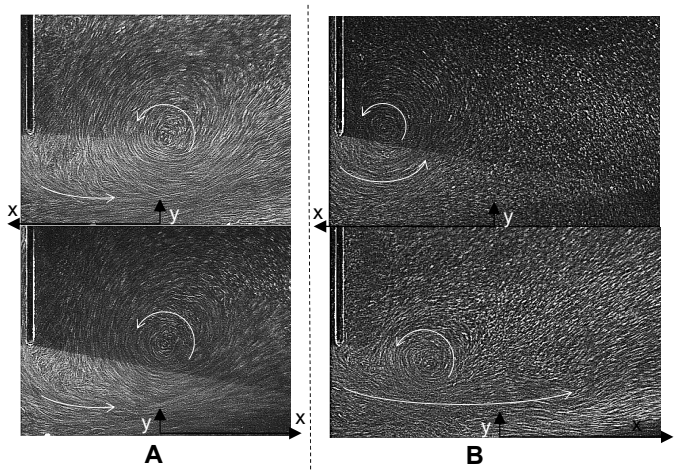

Fig. 3 Flow patterns: (A) symmetrical, $G = 40\ mm$, $A = 35\ mm$ and $f = 0,5\ Hz$, (B) asymmetrical: $G = 40\ mm$, $A = 14\ mm$ and $f = 1,0\ Hz$.

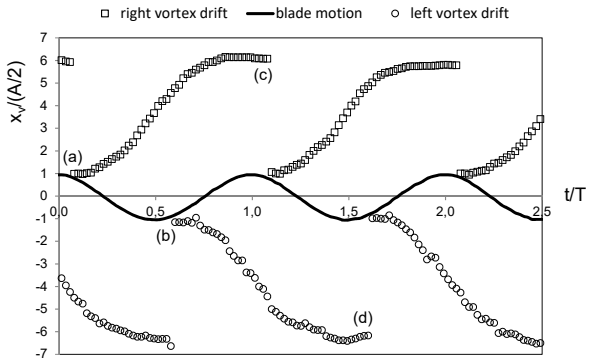

Fig. 4 Instantaneous horizontal position of the tip vortices ($\square, \circ$), x_v, and the horizontal displacement of the plate (continuous line) Labels (a), (b), (c) and (d) indicates the correlation between vortices motion and characteristic points of the plate path. Parameters are: $G = 30\ mm$, $A = 38.2\ mm$ and $f = 0.47\ Hz$.

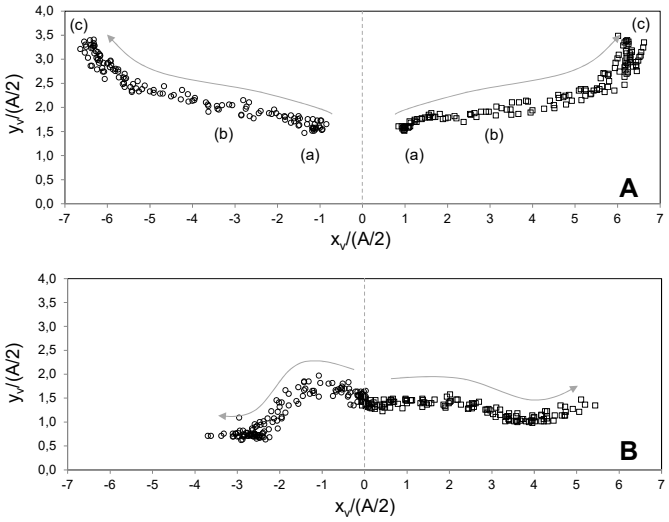

Fig. 5 Trajectory of the center of the tip vortex, (x_v, y_v), in physical space, for several oscillations. Parameters are: (A) symmetric flow (STS), $G = 30\ mm$, $A = 38.2\ mm$ and $f = 0.47\ Hz$; (B) asymmetric flow (TSSA), $G = 30\ mm$, $A = 38.2\ mm$ and $f = 1.52\ Hz$. Gray continuous lines indicates the path followed by the center of tip vortices.

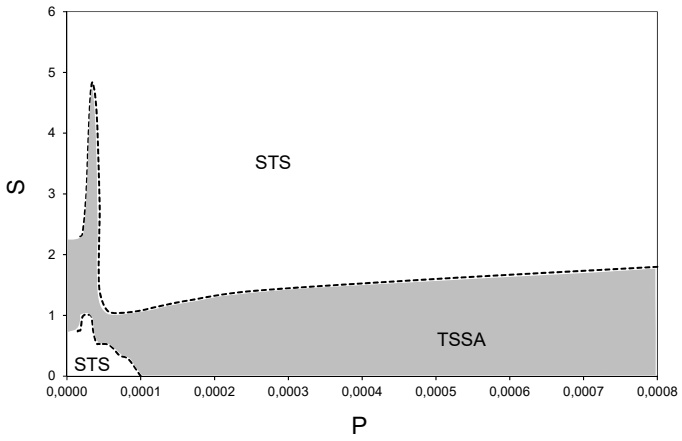

Fig. 6 Phase diagram of the flow patterns in the narrow cell, in terms of the dimensionless numbers $P = \nu T/H^2$ (see Eq. 5), in abscissa, and $S = \pi A/G$ (see Eq. 6), in ordinates.

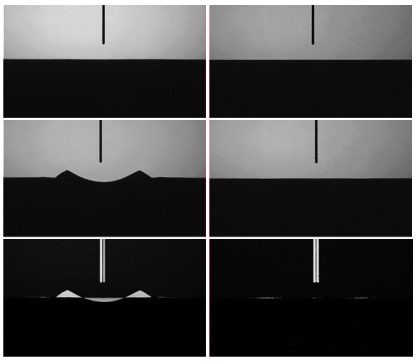

Fig. 7 Onset for sediment motion: the left column corresponds to a condition with $f > f_c$ (net sediment scouring is present), whereas the right column shows the condition close to the critical onset of sediment motion, $f \approx f_c$.

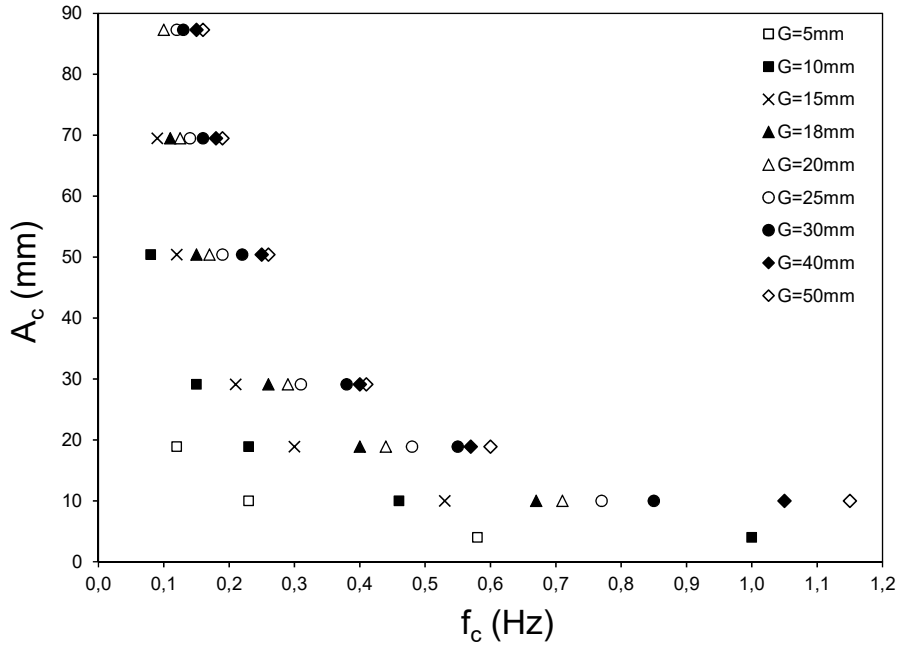

Fig. 8 The critical condition for the onset of sediment motion: curves for the critical amplitude, A_c, in ordinates, as a function of the critical frequency, f_c, in abscissa, for several values of gap, G.

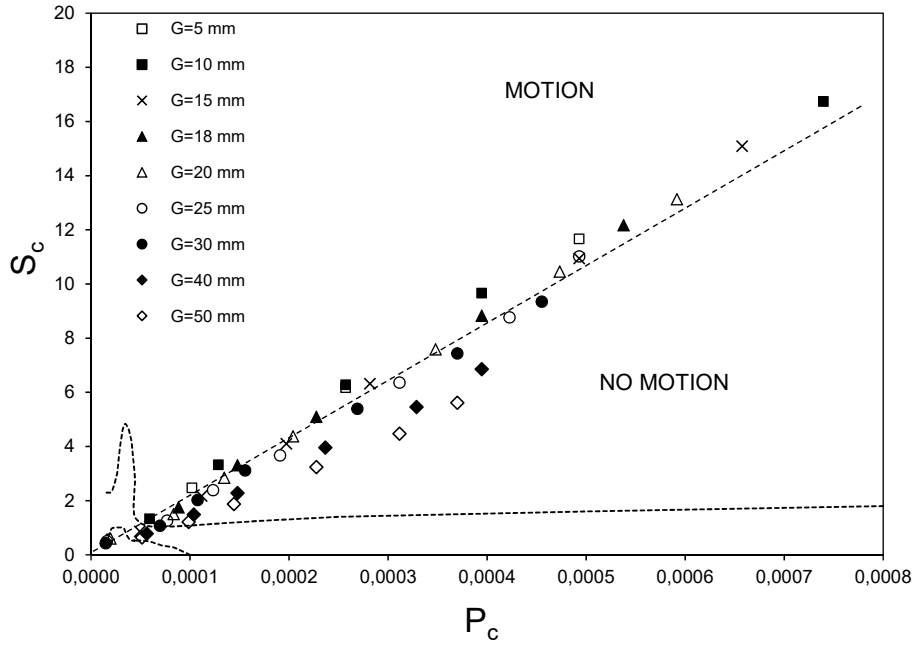

Fig. 9 Onset of sediment motion in the $S-P$ plane. In black dashed lines, the boundaries of the regions where symmetrical (STS) and asymmetrical (TSSA) flow structures are observed.

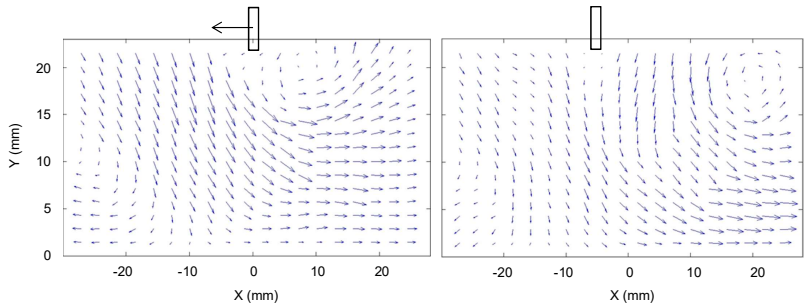

Fig. 10 Flow field measured with PIV below the plate for $G = 20\ mm$, $A = 10\ mm$ and $f = 0.5\ Hz$ with the plate in two locations in the cell. The plot at the left hand side corresponds to the plate in the center and moving toward the left end, and the plot at the right hand side corresponds to the plate at the left end of its path, prior to reversing its motion.

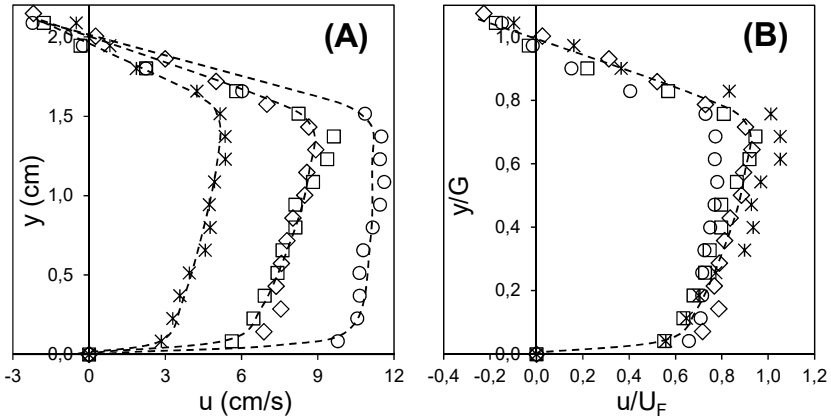

Fig. 11 Longitudinal velocity profiles below the plate, for $0 \leq y \leq G = 2\ cm$ and $x = 0$ (i. e., the plate is at the center of the cell). Markers are: $*A = 10.0\ mm\ f = 0.25\ Hz$, $\circ\ A = 29.1\ mm$ $f = 0.25\ Hz$, $\diamond\ A = 18.9\ mm\ f = 0.25\ Hz$ and $\square\ A = 10.0\ mm\ f = 0.50\ Hz$.

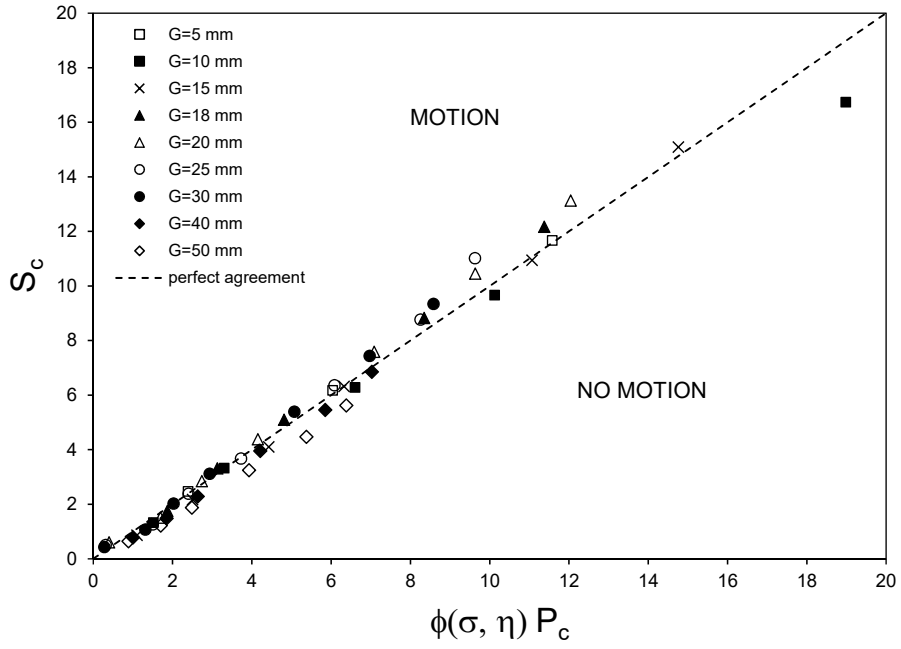

Fig. 12 The same data points as in Fig. 9 in terms of S_c and $\phi(\sigma, \eta)P_c$.